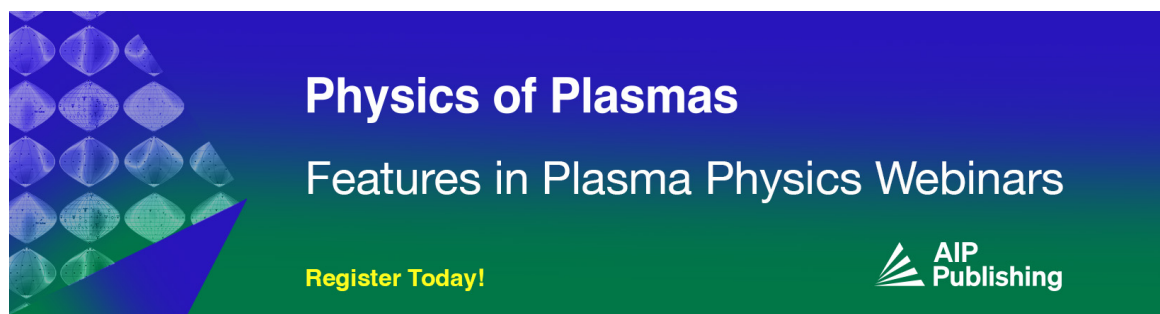# A computational study of pseudo-filamentary nanosecond pulsed dielectric barrier discharge in atmospheric air ⊘

Yanru Li (ID) ; Yulin Guo (ID) ; Yifei Zhu (ID) ; Anbang Sun ✉ (ID)

Check for updates

View Online

Export Citation

30 April 2024 09:25:26

A computational study of pseudo-filamentary nanosecond pulsed dielectric barrier discharge in atmospheric air

Yanru Li, (iD) Yulin Guo, (iD) Yifei Zhu, (iD) and Anbang Sun[a)] (iD)

AFFILIATIONS

State Key Laboratory of Electrical Insulation and Power Equipment, School of Electrical Engineering, Xi'an Jiaotong University, Xi'an 710049, People's Republic of China

[a)]Author to whom correspondence should be addressed: anbang.sun@xjtu.edu.cn

ABSTRACT

The formation and propagation of pseudo-filamentary dielectric barrier discharge in atmospheric air are investigated through a 2D fluid model. The discharge development can be divided into three stages: the volume streamer stage, the surface streamer stage, and the reverse discharge stage. The simulations show that the streamer head becomes wider and the electron density of the volume streamer head increases six times when the volume streamer interacts with the dielectric, and the volume streamer transforms into the surface streamer after the interaction. Compared with volume streamers, surface streamers have a smaller radius, a higher electric field, and a higher electron density. Furthermore, the parameters that may influence the discharge characteristics are also studied. It is found that a larger dielectric permittivity, a thinner dielectric, or a shorter voltage rise time leads to earlier inception of volume streamers, faster propagation of surface streamers, and higher current density. It is observed that the velocity of the surface streamer increases first, and then, decreases with the accumulated charges on the surface.

Published under an exclusive license by AIP Publishing. https://doi.org/10.1063/5.0120800

I. INTRODUCTION

As a source of low-temperature plasmas, dielectric barrier discharge (DBD) has the characteristics of non-equilibrium, mild discharge, and high electron energy. DBD has a simple discharge structure with a dielectric layer on at least one electrode; the discharge device has the advantages of easy sealing and low cost, which makes it widely used in industrial fields such as surface treatment,[1] ozone synthesis,[2] flow control,[3] plasma medicine,[4,5] and exhaust treatment.[6] According to the discharge morphology, it can be divided into filamentary mode and diffuse mode. The focus of this paper is on the filamentary DBD governed by the streamer mechanism.

Filamentary discharges ignite at the rising and falling edges of the applied voltage by the Laplacian field and the space charge field.[7] Some macroscopic properties of filamentary DBD have been studied experimentally.[7–14] Merbahi *et al.* found that each filamentary discharge spreads out like a funnel at the anode side,[8] and Liu and Neiger pointed out that the second discharge appeared almost at the same location as the previous one, which shows the memory effect.[15]

Numerical simulations have also been widely used to investigate microscopic properties, which are difficult to measure experimentally, such as electron and ion density distribution, the time-spatial evolution of the electric field, and electron energy. To adapt to different computational conditions and application objectives, computational methods such as fluid simulations,[16–21] circuit model-based simulations,[22–24] and PIC/MCC[25] are mainly developed at present. Because the results of fluid simulations are in good agreement with the experiment,[26] the simulation speed is fast, and the computational cost is low, it is commonly used. Braun *et al.* first proposed a fluid model for dielectric barrier discharge and divided the DBD development process into four stages: Townsend phase, ionization wave or streamer phase, cathode layer formation phase, and the decay phase.[20] Many of the subsequent simulation studies were based on it. Yurgelenas *et al.* pointed out that the non-uniformly distributed surface charge is decisive for the initiation of filament discharge through a 2D fluid simulation by assuming a Gaussian distribution of surface charge on the dielectric surface.[16,17] Papageorghiou *et al.* considered a small transition region of permittivity near the dielectric in plane-parallel electrode to ensure the numerical stability of the simulation[27] and compared the evolution of electric field when the permittivity changed linear and sigmoid in the single filamentary discharge. Celestin *et al.*
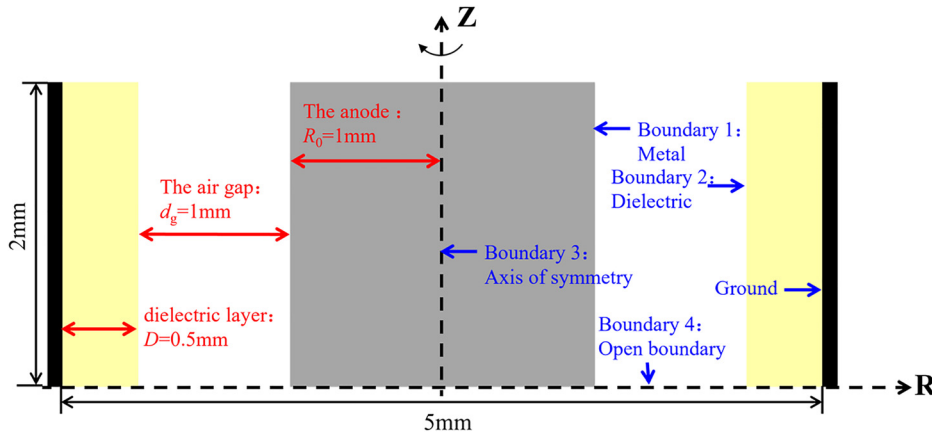
FIG. 1. Geometry used for simulation of a single DBD pseudo-filament. Gray is the high-voltage electrode (anode), yellow is the dielectric, and black is the ground electrode.

studied the effect of surface charges on the structure of the subsequent discharges in a rod-plane electrode in Ar.[28] Babaeva and Kushner investigated the ion energy distribution on dielectric surfaces in plane-parallel electrode; the ion energy was maximum when the discharge channel formed, and it gradually decreased during the propagation of the surface streamer, and it increased with the surface dielectric permittivity.[29]

Most properties of the discharge plasma are controlled by voltage excitation.[30] The nanosecond pulsed discharge has received attention over the recent decade,[7,11] and the high electric fields at the rising slop result in effective gas ionization, dissociation, and excitation, leading to a big current and a fast response, which can be used in electrochemical micromachining[31] and plasma medicine.[32,33] The main objective of this work is to simulate the propagation of pseudo-filamentary nsDBD and to investigate the effect of different parameters. A two-dimensional fluid simulation model is used to analyze the development of dielectric barrier discharge and the transition from volume streamer to surface streamer, and to discuss the similarities and differences between these two stages. Then, dielectric permittivity, dielectric thickness, and voltage rising rate are varied to study their effects on the current, initiation, and propagation velocity.

II. SIMULATION MODEL

A plasma solver PASSKEy (PArallel Streamer Solver with KinEtics) code coupling plasma and hydrodynamics has been used in this work. To simulate the discharge results under extremely inhomogeneous fields, the geometry is designed as a coaxial cylinder, which is widely used in industrial applications such as surface modification.[31] The simulations are performed in artificial air (20% O_2 and 80% N_2) in the atmospheric pressure. A two-dimensional axisymmetric model is established (see Fig. 1). The inner cylinder is the anode (the radius

R_0 is 1 mm), and the outer ring is the cathode (the inner R_1 and outer radius R_2 are 2 and 2.5 mm, respectively), with a dielectric layer of 0.5 mm and a permittivity of 4. The air gap is 1 mm. A pulsed voltage amplitude of 6 kV, rise time of 10 ns, and 40 ns full width at half maximum are applied to the high-voltage electrode. In this geometric assumption, the discharge is filamentary on the cross section and is a disk discharge in space. However, the characteristics of discharge are similar to the filamentary discharge. Therefore, the discharge simulated in this work is called pseudo-filamentary DBD.

Initial plasma density with Gaussian distribution is set on the anode surface to enable the pseudo-filamentary discharge to start smoothly, as shown in Eq. (1). The initial plasma has 0.2 mm on the R axis. The voltage starts at a higher value (3 kV) to facilitate streamer initiation,

$$n_{e0} = n_p = 10^{15} \times \exp\left(-\left(\frac{R\text{-}10^{-3}}{7.5\times10^{-5}}\right)^2 - \left(\frac{Z\text{-}10^{-3}}{3\times10^{-5}}\right)^2\right)$$
$$+ 10^{10}(\text{m}^{-3}). \tag{1}$$

The boundary conditions are summarized in Table I. The kinetic scheme can be seen in Table II, and this scheme contains 15 species, including charged, neutral, and excited species, and 34 reactions.

The detailed numerical method and validations of PASSKEy can be found in Refs. 26 and 40. The equations are briefly introduced here. First, the continuity equations combined with the drift-diffusion equations were solved to get the number density of different species,

$$\frac{\partial n_i}{\partial t} + \nabla \cdot \mathbf{\Gamma}_i = S_i + S_{\text{ph}}, \quad i = 1, 2, \ldots, N_{\text{total}}, \tag{2}$$

$$\mathbf{\Gamma}_i = -D_i \nabla n_i - (q_i/|q_i|)\mu_i n_i \nabla \Phi, \quad i = 1, 2, \ldots, N_{\text{charge}}, \tag{3}$$

where Φ is the electrical potential, n_i is the number density of species, and q_i is the charge of species. S_i is the source term for detailed

TABLE I. Boundary conditions in the simulation. The secondary electron emission coefficient γ is set to 0.01 for both metals and dielectrics.

	Metal	Dielectric	Open boundary
Potential	Anode: $\varphi = U(t)$ Cathode: $\varphi = 0$	$\partial \varphi / \partial t = 0$	$\cdots$
Flow toward boundary	$\partial \mathbf{\Gamma_e}/\partial n = 0, \partial \mathbf{\Gamma_i}/\partial n = 0$	charge accumulation	$\partial \mathbf{\Gamma_e}/\partial n = 0, \partial \mathbf{\Gamma_i}/\partial n = 0$
Flow away from the boundary	$\mathbf{\Gamma_e} = -\gamma\mathbf{\Gamma_i}, \mathbf{\Gamma_i} = 0$	$\mathbf{\Gamma_e} = -\gamma\mathbf{\Gamma_i}, \mathbf{\Gamma_i} = 0$	$\partial \mathbf{\Gamma_e}/\partial n = 0, \partial \mathbf{\Gamma_i}/\partial n = 0$

TABLE II. Kinetic scheme in the simulation.

No.	Reaction	Rate constant[a]	Ref.
R1	$e + N_2 \rightarrow N_2^+ + e + e$	$f(\sigma, \varepsilon)$	34
R2	$e + O_2 \rightarrow O_2^+ + e + e$	$f(\sigma, \varepsilon)$	34
R3	$e + N_2 \rightarrow e + N_2(A3\Sigma_u)$	$f(\sigma, \varepsilon)$	34
R4	$e + N_2 \rightarrow e + N_2(B3\Pi_g)$	$f(\sigma, \varepsilon)$	34
R5	$e + N_2 \rightarrow e + N_2(C3\Pi_u)$	$f(\sigma, \varepsilon)$	34
R6	$e + O_2 \rightarrow e + O + O$	$f(\sigma, \varepsilon)$	35,36
R7	$e + O_2 \rightarrow e + O + O(^1D)$	$f(\sigma, \varepsilon)$	35,36
R8	$N_2^+ + N_2 + M \rightarrow N_4^+ + M$	5×10^{-29}	35,37
R9	$N_4^+ + O_2 \rightarrow O_2^+ + N_2 + N_2$	2.5×10^{-10}	35,37
R10	$N_2^+ + O_2 \rightarrow O_2^+ + N_2$	6×10^{-11}	35,37
R11	$O_2^+ + N_2 + N_2 \rightarrow O_2^+ N_2 + N_2$	9×10^{-31}	37
R12	$O_2^+ N_2 + N_2 \rightarrow O_2^+ + N_2 + N_2$	4.3×10^{-10}	37
R13	$O_2^+ N_2 + O_2 \rightarrow O_4^+ + N_2$	1×10^{-9}	37
R14	$O_2^+ + O_2 + M \rightarrow O_4^+ + M$	2.4×10^{-30}	35,37
R15	$e + O_2 + O_2 \rightarrow O_2^- + O_2$	$2 \times 10^{-29} \times (300/T_e)$	37
R16	$e + O_2 \rightarrow O^- + O$	$f(\sigma, \varepsilon)$	36
R17	$O^- + O \rightarrow O_2 + e$	5×10^{-10}	38
R18	$O_2^- + O \rightarrow O_2 + O + e$	1.5×10^{-10}	39
R19	$e + N_4^+ \rightarrow N_2 + N_2(C3\Pi_u)$	$2 \times 10^{-6} \times (300/T_e)^{0.5}$	35
R20	$e + N_2^+ \rightarrow N + N + 2.25\,eV$	$2.8 \times 10^{-7} \times (300/T_e)^{0.5}$	38
R21	$e + O_4^+ \rightarrow O + O + O_2$	$1.4 \times 10^{-6} \times (300/T_e)^{0.5}$	35,37
R22	$e + O_2^+ \rightarrow O + O + 5.0\,eV$	$2 \times 10^{-7} \times (300/T_e)$	35,37
R23	$O_2^- + O_4^+ \rightarrow O_2 + O_2 + O_2$	1×10^{-7}	37
R24	$O_2^- + O_4^+ + M \rightarrow O_2 + O_2 + O_2 + M$	$2 \times 10^{-25} \times (300/T_{gas})^{3.2}$	37
R25	$O_2^- + O_2^+ + M \rightarrow O_2 + O_2 + M$	$2 \times 10^{-25} \times (300/T_{gas})^{3.2}$	37
R26	$O^- + N_2^+ \rightarrow O + N + N$	1×10^{-7}	38
R27	$N_2(C3\Pi_u) + N_2 \rightarrow N_2(B3\Pi_g, v) + N_2$	1×10^{-11}	35
R28	$N_2(C3\Pi_u) + O_2 \rightarrow N_2 + O + O(^1D)$	3×10^{-10}	35
R29	$N_2(C3\Pi_u) \rightarrow N_2 + h\nu$	2.38×10^7	37
R30	$N_2(B3\Pi_g) + O_2 \rightarrow N_2 + O + O$	3×10^{-10}	35
R31	$N_2(B3\Pi_g) + N_2 \rightarrow N_2(A3\Sigma_u) + N_2(v)$	1×10^{-11}	35
R32	$N_2(A3\Sigma_u) + O_2 \rightarrow N_2 + O + O$	$2.5 \times 10^{-12} \times (T_{gas}/300)^{0.5}$	35
R33	$O(^1D) + O_2 \rightarrow O + O_2$	$3.3 \times 10^{-11} \times \exp(67/T_{gas})$	35
R34	$O(^1D) + N_2 \rightarrow O + N_2$	$1.8 \times 10^{-11} \times \exp(107/T_{gas})$	35

[a]Rate constants are given in s^{-1}, $cm^3\,s^{-1}$, and $cm^6\,s^{-1}$. Electron temperature T_e is given in K. Gas temperature T_{gas} is given in K.

chemical reactions. S_{ph} is the photoionization source term for electrons and oxygen ions. D_i and μ_i are the diffusion coefficient and the mobility of charged species i. Γ_i is the flux of species. For the transport equations, an explicit UNO3 scheme (third order in time and space) coupled with the Strang operator for spatial splitting is used[41] to solve the drift term, an explicit second order central discretization scheme is used to solve the diffusion term, while for chemistry, the stabilized Runge–Kutta–Chebyshev scheme is used.[42] The photoionization model is based on the assumption that the major contribution to the rate of photoionization comes from the radiation in the spectral range 98–102.5 nm, and the photoionization source term S_{ph} is calculated by Helmholtz equations,

$$S_{ph} = \sum_j S_{ph}^j, \qquad (4)$$

$$\nabla^2 S_{ph}^j - (\lambda_i p_{O_2})^2 S_{ph}^j = -A_j p_{O_2}^2 I(R), \qquad (5)$$

$$\frac{g(R)}{p_{O_2}} = (p_{O_2} R) \sum_j A_j e^{-\lambda_i p_{O_2} R}, \qquad (6)$$

where p_{O_2} is the partial pressure of O_2, $I(R)$ is the ionization source rate, $\frac{g(R)}{p_{O_2}}$ is the photoionization function, λ_j and A_j are fitting coefficients for photoionization functions obtained in experiments and taken from Ref. 43.

Second, Poisson's equations were solved to get the distribution of potential and electric field,

$$-\nabla(\varepsilon\nabla\Phi) = \sum_{i=1}^{N_{ch}} q_i n_i. \qquad (7)$$

Poisson's equation and Helmholtz equations are solved by a pre-conditioned conjugate-gradient solver, and a semi-implicit time integration scheme was used for Poisson's equation.[44–47] The charge flux flowing toward the dielectric is stored in the edge of the mesh cell, and the detailed numerical realization method of dielectric–gas interface is as follows. At the dielectric–gas interface, the electric potential is continuous, but the axial electric field is not. If there is a deposition of surface charges on a dielectric surface, the jump condition for normal electric field E on the interface of two dielectrics of permittivity ε_1 (defined in cell i, j) and ε_2 (defined in cell $i+1, j$) with surface charges ρ located at the interface between the two dielectrics is Eq. (8). If there is no surface charge, $\rho = 0$,

$$-\varepsilon_1 E_1 + \varepsilon_2 E_2 = \rho. \qquad (8)$$

The traditional Poisson's equation (7) is integrated over the volume element $V_{i,j}$ of the cell (i, j) using the Gauss–Ostrogradsky theorem, as shown in Eq. (9), and in combination with Eq. (8), the product of ε and the flux of the electric field on the surface of the dielectric without and with surface charge can be obtained as Eqs. (10a) and (10b),

$$\oint_S (\varepsilon(-\nabla\Phi)) \cdot \boldsymbol{n} dS = V_{i,j}\rho = f(E), \qquad (9)$$

$$f_1(E) = S_{i+1/2,j} \frac{\varepsilon_2\varepsilon_1(\Phi_i - \Phi_{i+1})}{\varepsilon_2(x_{i+1/2} - x_i) + \varepsilon_1(x_{i+1} - x_{i+1/2})}, \qquad (10a)$$

$$f_2(E) = S_{i+1/2,j} \frac{\varepsilon_2\varepsilon_1(\Phi_i - \Phi_{i+1})}{\varepsilon_2(x_{i+1/2} - x_i) + \varepsilon_1(x_{i+1} - x_{i+1/2})}$$
$$- S_{i+1/2,j} \frac{\rho(x_{i+1/2} - x_i)(x_{i+1} - x_{i+1/2})}{\varepsilon_2(x_{i+1/2} - x_i) + \varepsilon_1(x_{i+1} - x_{i+1/2})}. \qquad (10b)$$

When the surface charge is included, an additional source about the surface charge density ρ is added to the right-hand side of the equation only at the point (i, j) and $(i+1, j)$.

III. RESULTS AND DISCUSSION

A. The evolution of dielectric barrier discharge

The voltage and current profiles are shown in Fig. 2. V_a is the applied voltage, starting from 3 kV. V_d is the voltage across the dielectric. In the modeling, the current is calculated as an integral of fluxes of negative and positive charges through the surface of the anode. The displacement current, which depicts the change rate of the electric displacement field ($\boldsymbol{D}$), is not calculated in our simulation, because it does not help describe the discharge characteristics and does not affect the discharge results. It can be seen that the current pulse is generated on the rising and falling edges of the voltage pulses, corresponding to two discharges, which is consistent with the results in early experiments of nanosecond pulsed dielectric barrier discharge,[9,15] whether the discharge is the diffuse mode at atmosphere with a special designed DBD
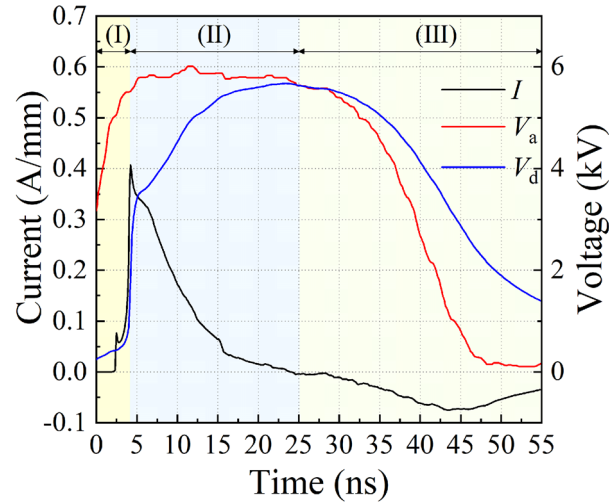

FIG. 2. Waveform of voltage and current. The black line is the current waveform. The red line is the applied voltage, 6 kV amplitude, 10 ns is the rise time, and 40 ns full width at half maximum. The blue line is the voltage across the dielectric.

configuration[9] or in the filamentary mode at low pressure (50 mbar) with the knife-plane configuration.[15]

The discharge development can be divided into three stages: (I) the volume streamer stage (before 4.2 ns), (II) the surface streamer stage (4.2–25 ns), and (III) the reverse discharge stage (25–55 ns).

(I) *The volume streamer stage.* V_a and the current are both in their rising phase, but V_d is a small value. The current peaks at about 4.2 ns with a value of 0.41 A/mm. At the same time, the volume streamer breaks down the air gap (Fig. 3, 4.2 ns), and V_d starts increasing. Electrons flow into the anode and shrink toward the streamer around 2.5 ns, and the electron density in the non-streamer region (that is Z > 1.2 mm and Z < 0.8 mm) near the anode decreases from $\sim 2.6 \times 10^{16}$ m^{-3} at 2 ns to $\sim 1.5 \times 10^{16}$ m^{-3} at 2.5 ns, resulting in a slight drop in current and a local current peak.

(II) *The surface streamer stage.* After the volume streamer breakdown, surface streamers form and propagate along the dielectric surface, as shown in Figs. 3 and 4. During the surface streamer stage, V_a is almost constant, the current gradually decreases to 0, and V_d increases to 5.7 kV at the end of this stage. This is caused by a decreasing electric field in the gap. The accumulation of positive ions on the surface forms a space charge field that weakens the electric field in the gap and enhances the electric field in the dielectric (Fig. 4). Therefore, discharges gradually extinguish with a gradually decreasing current.

(III) *The reverse discharge stage.* The cause of the reverse discharge is different from that of the first discharge (before 25 ns, both the volume and the surface streamer stage). The first discharge is ignited because the voltage across the gap reaches the breakdown threshold, while the reverse discharge is ignited because the space charge field is very strong when V_a drops. The reverse discharge occurs at
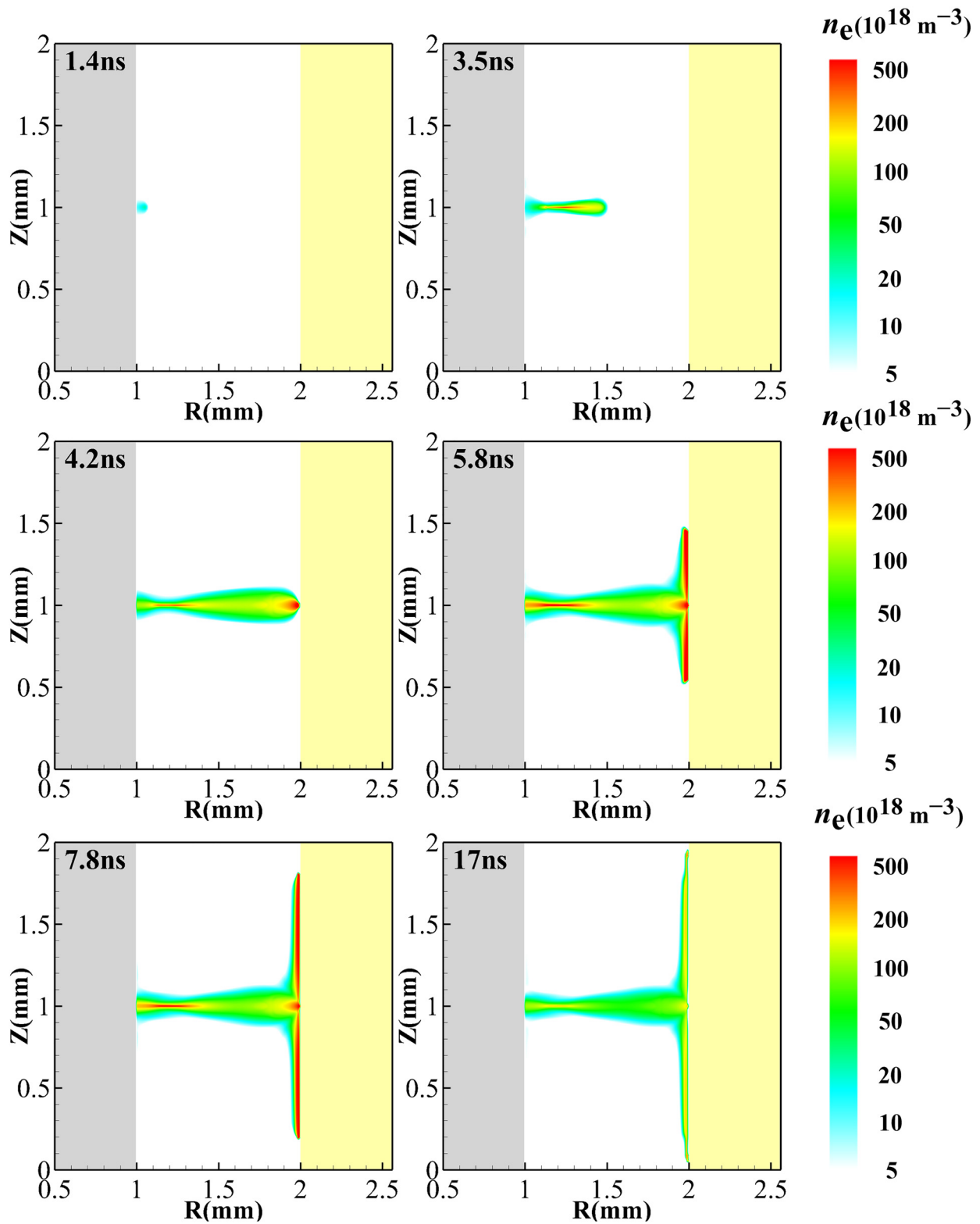
FIG. 3. Streamer development process before 17 ns. The air gap is 1 mm. The dielectric layer is 0.5 mm with $\varepsilon_r = 4$.
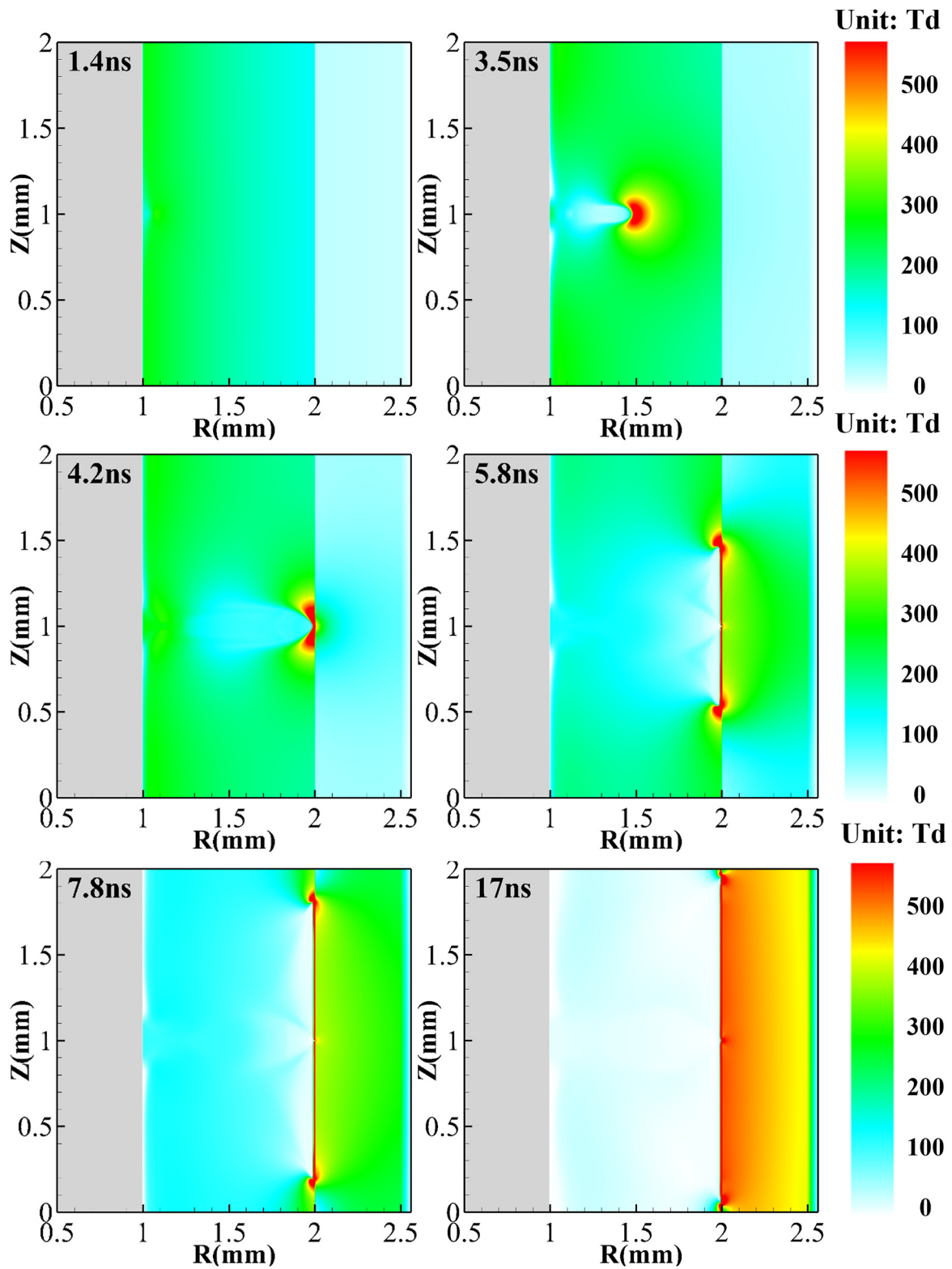
FIG. 4. Spatial distribution of the electric field before 17 ns.
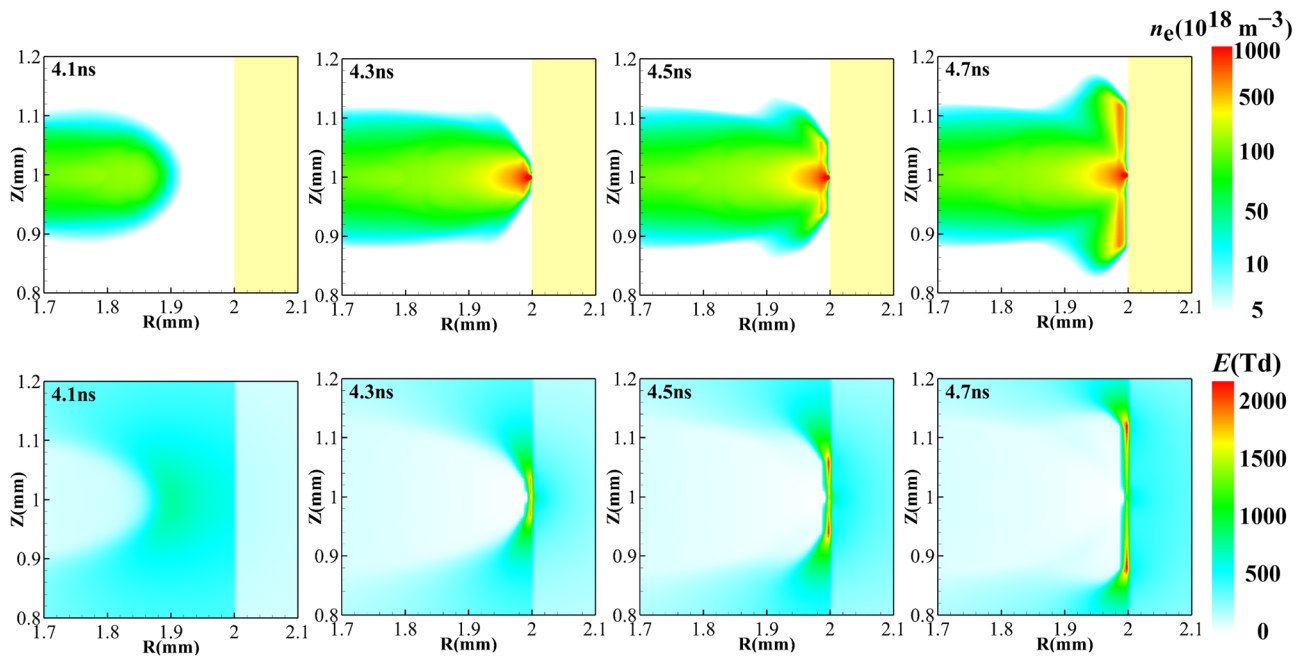
30 April 2024 09:25:26

FIG. 5. Spatial distribution of electron density and electric field when the volume streamer crosses the gap and interacts with the dielectric.

25 ns, at the falling edge of V_a. The amplitude of the reverse discharge current is 0.073 A/mm, smaller than that of the first discharge (0.41 A/mm), which is consistent with the results of the one-dimensional helium simulation[48] and the results in plane-parallel electrodes under airflow in the experiment.[49] In addition, the reverse discharge current has a duration of 30 ns, longer than that of the first one (23 ns).[50] We believe that the long voltage drop time is to blame for this.

The discharge transforms from a volume streamer to a surface streamer when the volume streamer interacts with the dielectric. Figure 5 shows the electron density evolution of the volume streamer head when it interacts with the dielectric. The head is in the shape of a water drop when the streamer propagates in the gas gap. When the volume streamer arrives at the dielectric, it deflects and continues propagating along the dielectric. Electrons move from the collision point to both positive and negative directions of the Z axis, and they gradually develop into surface streamers, as shown in Fig. 5 (5.8 ns). At the same time, the maximum electron density increases ∼six times in our cases (from ∼1×10^{20} to ∼7×10^{20} m^{-3}), and the head becomes wider (maximum diameter from 0.22 to 0.27 mm) with a flat shape. In addition, a sheath layer about 6 μm is formed between the surface streamer and the dielectric, in which the electric field is generally larger than 1500 Td, and the maximum is above 2000 Td. During this process, the dielectric acts as a capacitor to accumulate charged ions, forming the space charge field that weakens the total electric field. Thus, avoiding the generation of more severe discharges and forming a more stable discharge.

There are several differences between volume streamers and surface streamers.

(A) Their shapes are different. The volume streamer has a growing diameter during the propagation. It is in the shape of a water drop, and the maximum diameter is 0.22 mm just before interacting with the dielectric. While the surface streamer is flat, the maximum diameter is 0.06 mm, much smaller than the volume streamer.

(B) The electric field distributions are different. Figure 6(a) shows the electric field evolution in the volume streamer ($Z = 1$ mm). The head electric field is 712 Td at 2.6 ns, and a gradual decrease happens as the streamer propagates toward the dielectric. Then, the electric field becomes stronger when the streamer is very close to the dielectric after 3.8 ns, and it rises sharply to about 1300 Td when the volume streamer interacts with the dielectric at 4.2 ns. The change of the head electric field is related to the initial plasma density. As shown in Fig. 3, a "bottleneck" is formed in the volume streamer at $Z = 1.2$ mm, it provides a large electron density and a large electric field so that the volume streamer can develop forward, especially when it is just formed. At 2.6 ns, the streamer is in the bottleneck area, and the head electric field reaches the local maximum (712 Td) at 1.23 mm, indicating that the volume streamer is formed. The electrons are mainly generated by the bottleneck in this stage. Then from 2.6 to 3.8 ns, the streamer head gradually moves away from the bottleneck, and the head electric field gradually decreases with the development of the volume streamer. The head of the streamer expands, and the electrons are mainly generated by the head. Finally, the head electric field increases after 3.8 ns due to potential compression when the streamer approaches the cathode dielectric. Figure 6(b) shows the surface streamer's electric field evolution, which is obtained from $R = 1.985$ mm. The strongest electric
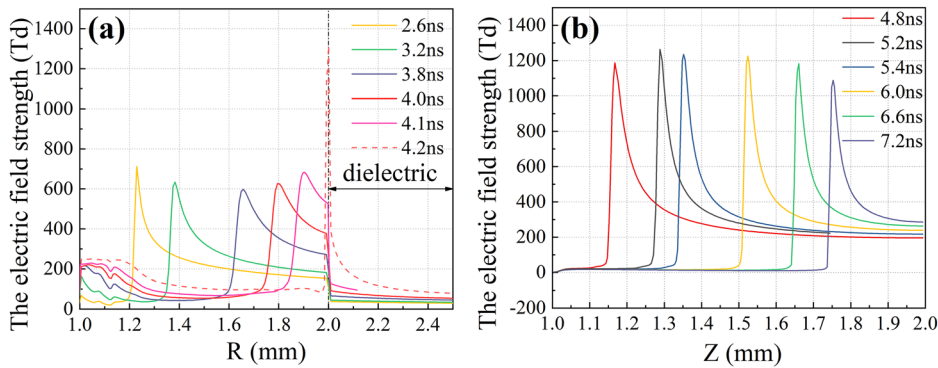
FIG. 6. Electric field strength changing process of (a) volume streamer and (b) surface streamer.

field also appears at the head (about 1200 Td). It is worth noting that the maximum electric field of the surface streamer is twice that of the volume streamer. During the propagation of the surface streamer, the electric field increases slightly first and then decreases, which is consistent with the results of plane-parallel DBD in Refs. 25 and 29.

(C) The electron densities are different. The electron density of the surface streamer is higher, as shown in Fig. 3; the maximum electron density of the volume streamer is about $3 \times 10^{20} \, m^{-3}$, while the maximum electron density of the surface streamer is about $7 \times 10^{20} \, m^{-3}$. This is due to the different ionization strength at the streamer head. When the electric field doubles, the ionization strength increases by an order of magnitude. In other words, the difference in electric field leads to the difference in electron density between the volume streamer and the surface streamer.

(D) The velocities are different. Figure 7 shows the streamers velocities in two stages. Although their velocities are in the same order of magnitude, their propagation processes are different. For the volume streamer [Fig. 7(a)], the closer the volume streamer gets to the dielectric, the faster the velocity. For the surface streamer [Fig. 7(b)], the velocity can be divided into three phases: initial phase (4.2–5 ns), propagation phase (5–10 ns), and stagnate phase (above 10 ns). In the initial phase, the velocity increases to $0.32 \, mm \cdot ns^{-1}$ with the diffusion of the volume streamer. In the propagation phase, it propagates from 1.24 to 1.91 mm with an average propagating velocity of $0.134 \, mm \cdot ns^{-1}$, and the velocity becomes slower when more and more space charges are accumulated on the dielectric surface. Similar trends in velocity, which grows up first and then slows down, are also observed in nanosecond surface dielectric barrier discharge (nSDBD).[26] But this can hardly be observed
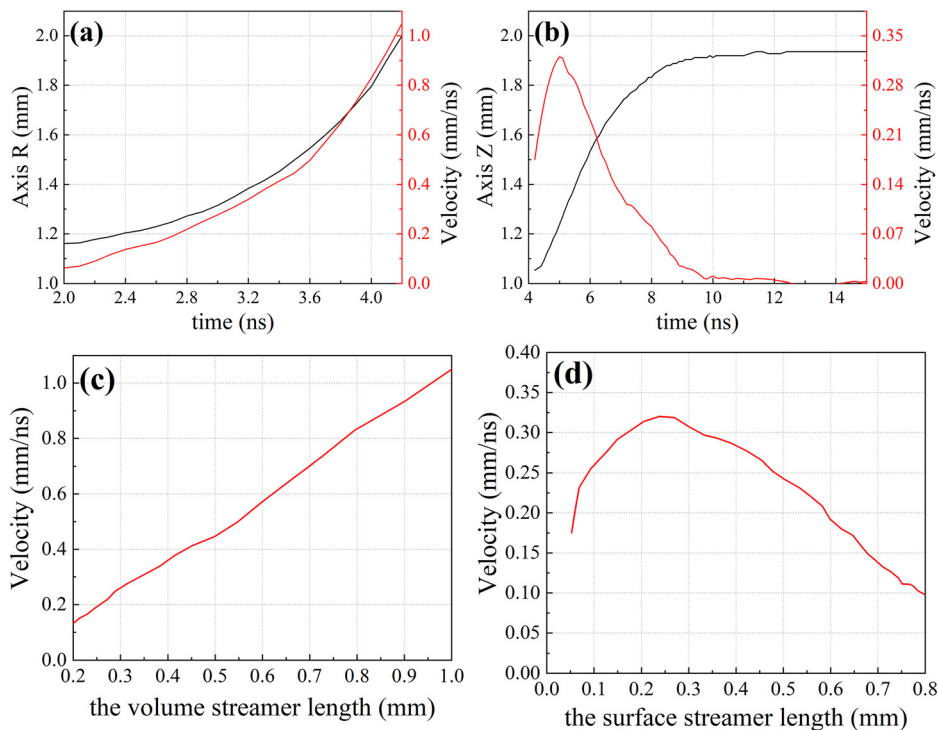

FIG. 7. Position of streamer head and its velocity of (a) volume streamer and (b) surface streamer. (c) Volume streamer velocity vs its length. (d) Surface streamer velocity vs its length.

TABLE III. Parameters and their values.

Section	Dielectric permittivity (ε_r)	Dielectric thickness (D)	Voltage rising rate (v_r)
1	(2, 3, 4)	0.5 mm	0.6 kV/ns
2	4	(0.5, 0.6, 0.8) mm	0.6 kV/ns
3	4	0.5 mm	(0.4, 0.6, 1.2) kV/ns

in experiment because the rising phase of surface streamer velocity only lasts about 1 ns, and it is very difficult to diagnose this phenomenon during such a short time in experiments. In the stagnate phase, the streamer does not move forward, and the electron density decreases, as shown in Fig. 3. During the whole discharge process, the velocity of the surface streamer is smaller than that of the volume streamer, which is similar to the simulation results of Papagorghiou et al.[27]

B. The effect of different parameters

In this section, we systematically study the effect of several parameters on the dielectric barrier discharge: the dielectric permittivity, the dielectric thickness, and the voltage rising rate. Their values are shown in Table III.

1. The effect of dielectric permittivity

The dielectric permittivity (ε_r) is set as 2, 3, and 4, respectively, to study its effect on DBD. In addition, the dielectric thickness is 0.5 mm, and the voltage rising rate is 0.6 kV/ns.

a. Effect on the discharge current. Figure 8 shows the different current profiles. The volume streamer breaks down the gap earlier (from 5.1 to 4.2 ns) when the dielectric permittivity increases. Furthermore, the current peak value almost doubles when the permittivity doubles. The proportional relationship between current and permittivity is also verified at low pressure in plane-parallel configuration.[51] Changing the relative permittivity will not directly affect the electric field at the head of the volume streamer, but will directly affect the value and spatial distribution of the Laplacian field. In particular, when the filamentary streamer is not yet formed, the space charge field is small and the Laplacian field plays a major role in promoting the ionization. Figure 9(a) shows the potential
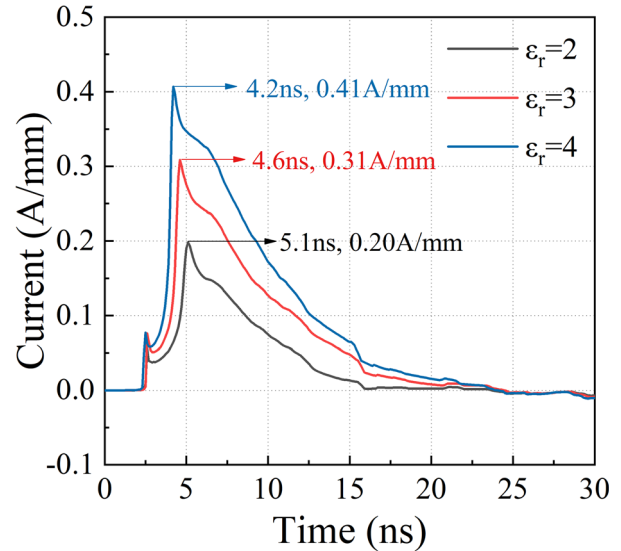

FIG. 8. Current vs time for dielectrics with relative permittivities ε_r of 2, 3, and 4.

and Laplacian field distribution of $Z = 1$ mm at 3 ns (i.e., the moment when the current starts increasing), and Fig. 9(b) shows that at the time of breakdown (i.e., the moment when the current reaches its peak). The potential goes down faster, and the Laplacian field increases when the permittivity is larger. Collisions between species are more intense, and electron mobility is larger. Therefore, the current increases with the permittivity.

b. Effect on the inception of volume streamer. The maximum electron density increases to 2×10^{19} m^{-3} when the permittivity increases to 4 at 1.4 ns, but the electron density is below 5×10^{18} m^{-3} when the permittivity is 2, as shown in Fig. 10. The discharge ignites earlier when the permittivity increases. In the non-ignited case, the DBD arrangement can be interpreted as two capacitors connected in series, one is the dielectric capacitance C_d and the other is the gas gap capacitance C_g. The coaxial cylindrical capacitor can be calculated by the following equations:

$$C_d = \frac{Q}{V_d} = \frac{2\pi\varepsilon_0\varepsilon_r L}{\ln R_2 - \ln R_1}, \quad (11a)$$
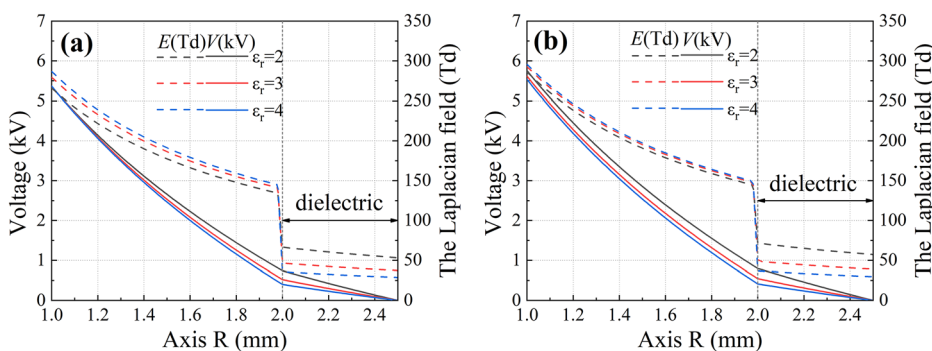

FIG. 9. Potential and Laplacian field distribution of $Z = 1$ mm (a) at 3 ns and (b) at the time of breakdown with relative permittivities ε_r of 2, 3, and 4.
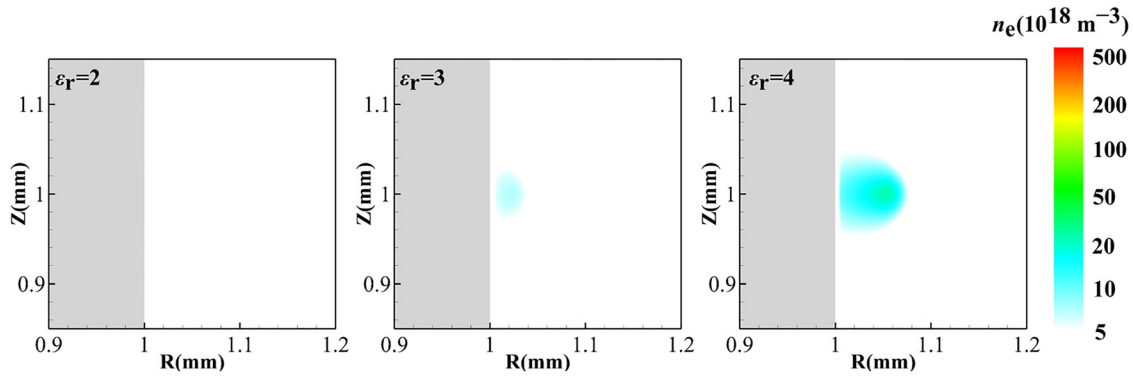
FIG. 10. Spatial distribution of electron at 1.4 ns with relative permittivities ε_r of 2, 3, and 4.

$$C_g = \frac{Q}{V_g} = \frac{2\pi\varepsilon_0 L}{\ln R_1 - \ln R_0}, \qquad (11b)$$

where R_1 and R_2 are the inner and outer radii of the outer ring, respectively, R_0 is the radius of the inner cylinder, and L is the length of the cylinder. The capacitance increases linearly with the permittivity when the geometric parameters are the same. The dielectric capacitance C_d becomes larger, while the gas gap capacitance C_g keeps constant when the permittivity increases from 2 to 4. Therefore, the voltage across the gas gap V_g is higher, and the voltage across the dielectric V_d is lower (as shown in Fig. 11), resulting in the electric field being stronger before the volume streamer formed, which is the main reason that the discharge ignites earlier with a larger permittivity.

c. Effect on the electric field. Since relative permittivity will lead to the change of discharge initiation and velocity, the electric field and electron density distribution at the same position is compared ($Z = 1.6$ mm), as shown in Fig. 12. The electric field in the sheath near the heads grows up from 1000 to 2000 Td with an increasing permittivity from 2 to 4. A similar trend of the electric field has been observed in the streamer discharge mode of DBD at 100 mbar in Ref. 51. This can be explained in terms of capacitive charging. Dielectric capacitors with large capacity charge slower, and more concentrated voltage is available for the surface streamer head and sheath, resulting in the electric field being stronger. The distribution of electron density on the surface of a dielectric is shown in Fig. 12(b) that the larger the relative permittivity, the larger the electron density.

d. Effect on surface streamer velocity. Figure 13(a) shows the position of the streamer head with different permittivities. The volume streamer interacts with the dielectric earlier with a larger permittivity. The surface streamer tends to be stable after 10 ns. The maximum distance that the surface streamer could reach increases by 0.05 mm (from 1.88 to 1.93 mm) when the permittivity increases from 2 to 4. Figure 13(b) shows the streamer velocity. The inflection points occur at $Z = 1.3$ mm in all three cases, within 1 ns of surface streamer initiation. The change of surface streamer velocity is closely related to the electric field. Take $\varepsilon_r = 4$ as an example, the electric field increases first and then decreases, and reaches its maximum at 5.2 ns (Fig. 6). Therefore, the surface streamers get faster with increasing electric field, and then gradually decrease with decreasing electric field. In addition, the velocities of surface streamers increase with permittivity. The same relationship between permittivity and the surface streamer velocity is also reported in Ref. 52 when the permittivity changes from 2 to 5, although their configuration is a pin-plane electrode with a horizontal dielectric in between.

2. The effect of dielectric thickness

The dielectric thickness (D) is set to 0.5, 0.6, and 0.8 mm, respectively, to study its effect on DBD. In addition, the dielectric permittivity is 4, and the voltage rising rate is 0.6 kV/ns.

a. Effect on the discharge current. Figure 14 shows the current profiles with different dielectric thicknesses. A higher discharge peak
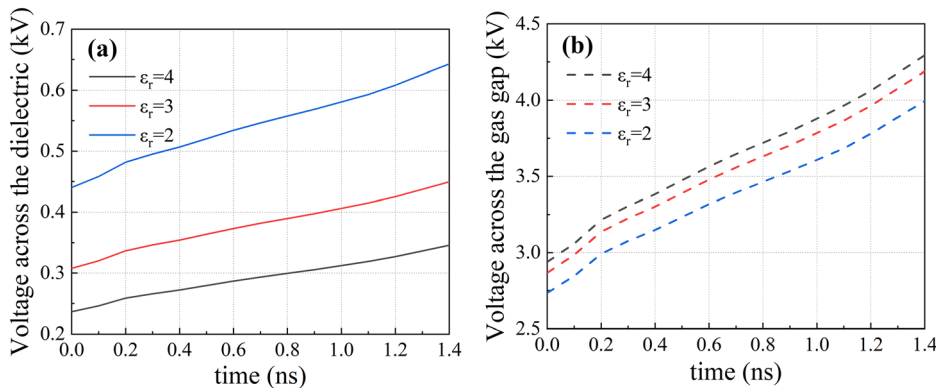

FIG. 11. Voltage across (a) the dielectric and (b) the gas gap with relative permittivities ε_r of 2, 3, and 4.
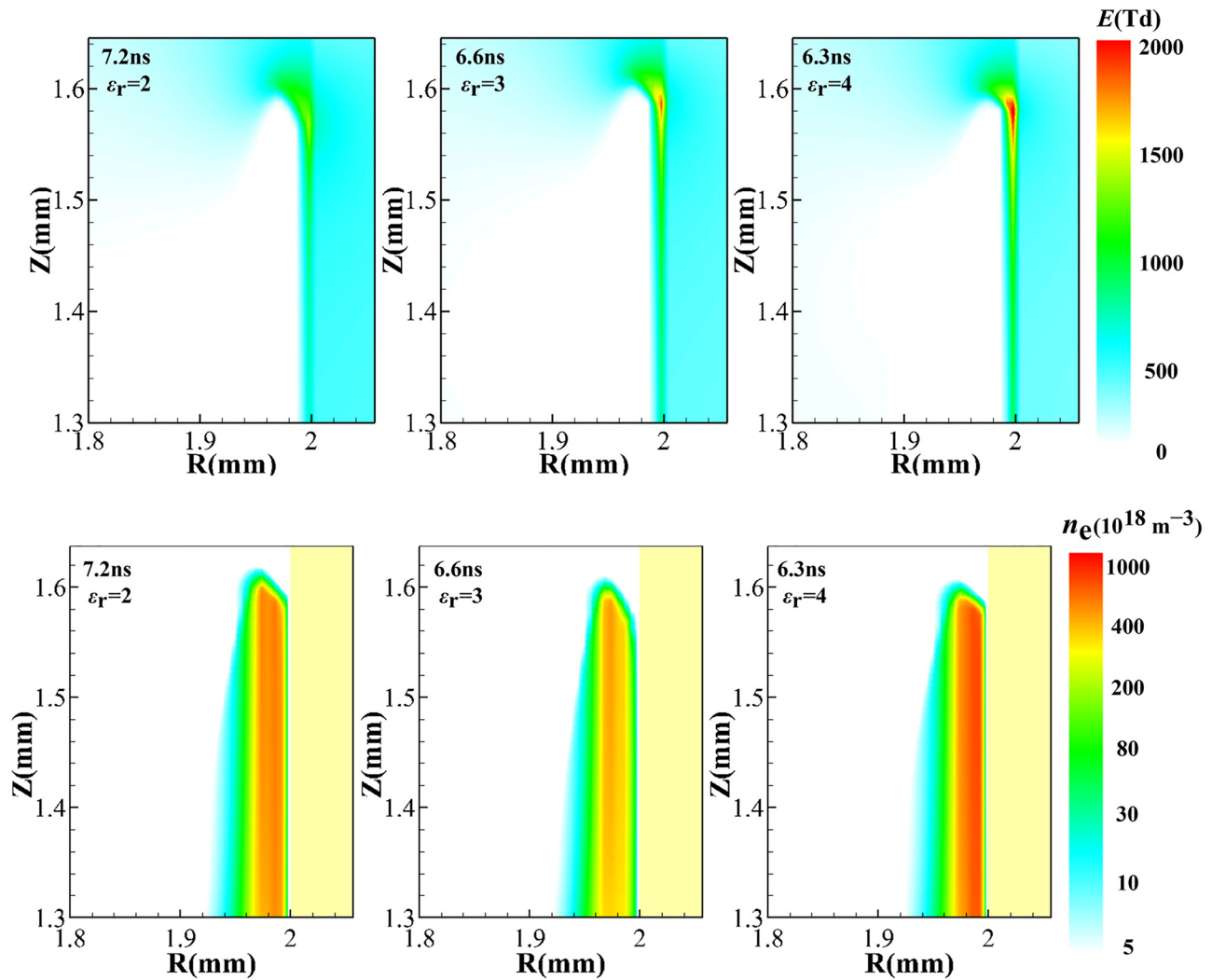
FIG. 12. Electric field distribution and electron density distribution of the surface streamers when the streamer heads are at $Z = 1.6$ mm with relative permittivities ε_r of 2, 3, and 4.
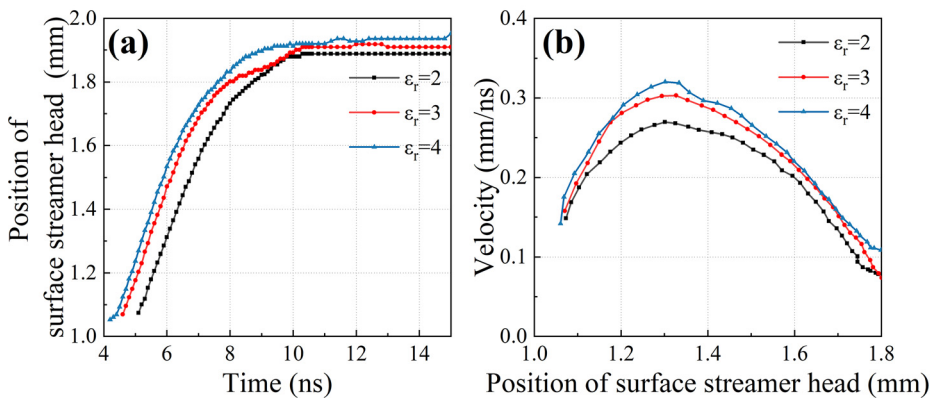

FIG. 13. (a) Position of surface streamer head vs time (b) streamer velocities vs their position for different relative dielectric permittivities.
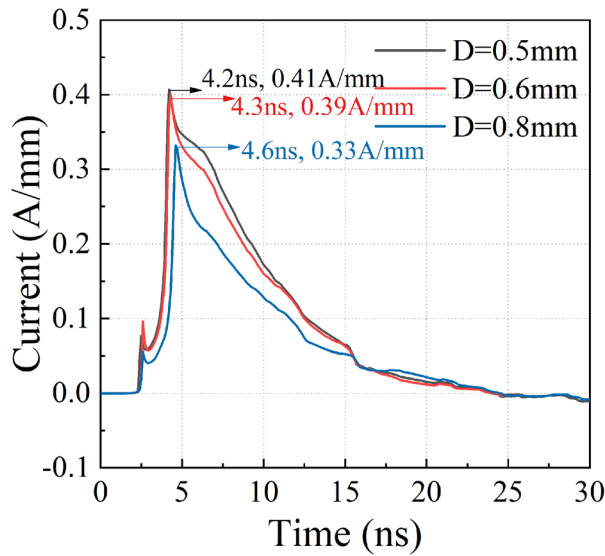
FIG. 14. Current vs time for dielectrics with a thickness of 0.5, 0.6, and 0.8 mm.

and an earlier breakdown appear when the thickness decreases. The effect mechanism is the same as that of the permittivity, and this is also related to the Laplacian field. The potential goes down faster, and the Laplacian field is larger with the thinner dielectric, as shown in Fig. 15. The collisions will be more intense, and electron mobility will be faster in a large field, directly resulting in larger current.
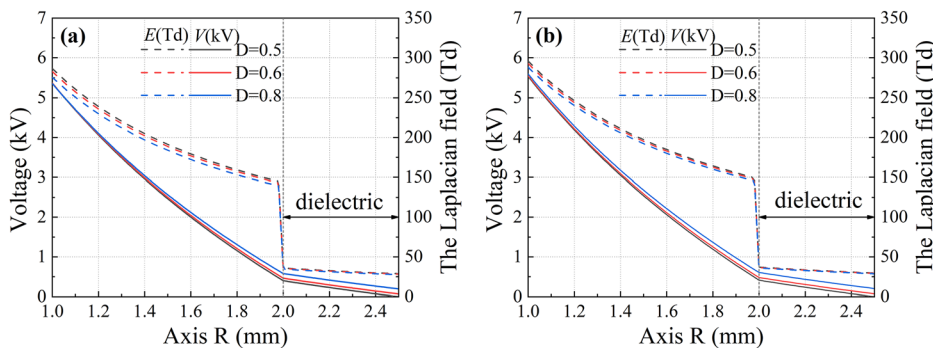
b. Effect on the inception of volume streamer. The electron density decreases by about an order of magnitude (from 2×10^{19} to 4×10^{18} m^{-3}) when the dielectric thickness increases from 0.5 to 0.8 mm at 1.4 ns, as shown in Fig. 16. It means the volume streamer will ignite later when the dielectric thickness increases to 0.8 mm. This can also be explained by the capacitance properties of DBD before discharge igniting. The dielectric capacitance C_d becomes smaller, while the gas gap capacitance C_g remains constant when the dielectric thickness increases, as shown in Eq. (11). Therefore, the voltage across the gas gap V_g is lower (as shown in Fig. 17), resulting in the electric field in the gap being weaker before the volume streamer developed, so the discharge ignites later.

c. Effect on surface streamer velocity. Figure 18 shows the velocity with different dielectric thicknesses. The maximum distance that the surface streamer could reach decreases with increasing dielectric thickness [Fig. 18(a)]. The velocity also increases when the dielectric thickness is thinner [Fig. 18(b)]. It can be seen that the inflection points occur at almost the same position ($Z \approx 1.3$ mm) when the dielectric thickness is 0.5 or 0.6 mm, but it occurs at 1.25 mm when the thickness is 0.8 mm.

3. The effect of voltage rising rate

The voltage rising rate (v_r) is set as 0.4, 0.6, and 1.2 kV/ns, respectively, to study its effect on the discharge. In addition, the dielectric permittivity is 4, and the dielectric thickness is 0.5 mm.

a. Effect on the discharge current. Figure 19 shows the variation of the current profile. A faster rising rate leads to an earlier breakdown in the gap and a larger current peak, this is almost universal.[48,53,54]

FIG. 15. Potential and Laplacian field distribution of $Z = 1$ mm (a) at 3 ns and (b) at the time of breakdown with a thickness of 0.5, 0.6, and 0.8 mm.
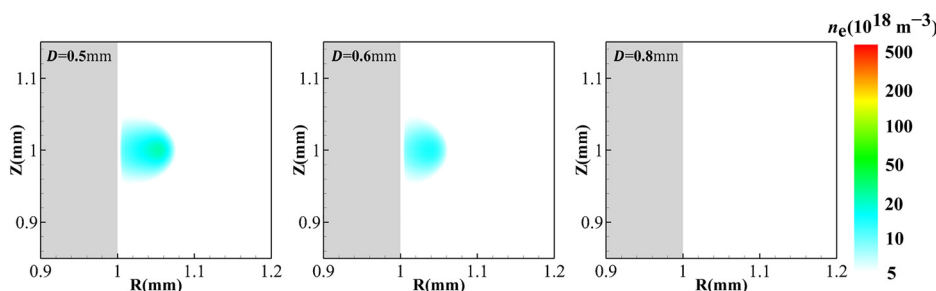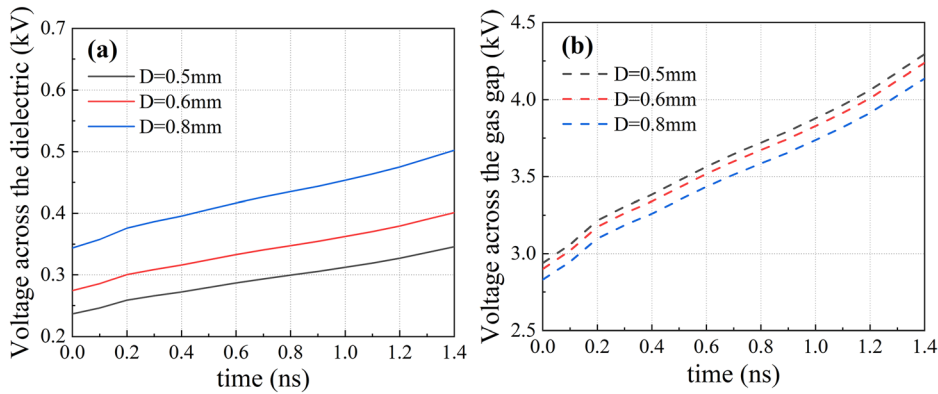

FIG. 16. Spatial distribution of electrons at 1.4 ns with a dielectric thickness of 0.5, 0.6, and 0.8 mm.

FIG. 17. Voltage across (a) the dielectric and (b) the gas gap with a thickness of 0.5, 0.65, and 0.8 mm.
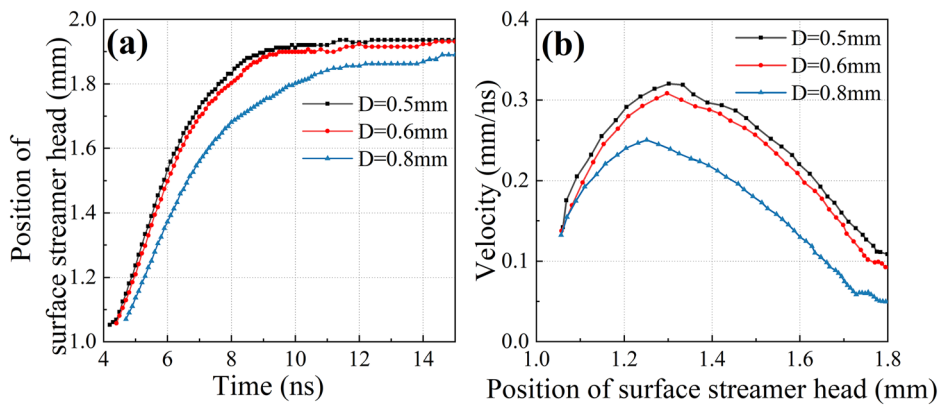

FIG. 18. (a) Position of surface streamer head vs time (b) streamer velocities vs their position with a dielectric thickness of 0.5, 0.6, and 0.8 mm.
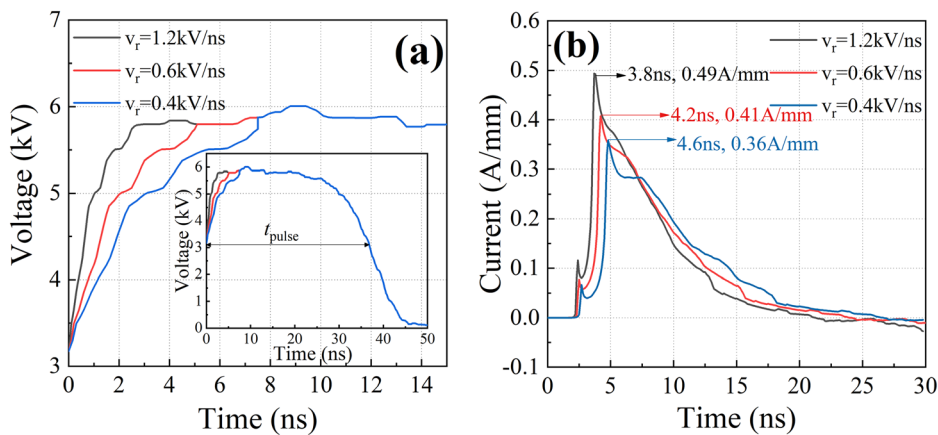

FIG. 19. (a) Voltage and (b) current vs time with a voltage rising rate of 0.4, 0.6, and 1.2 kV/ns.

A faster rising rate leads to a higher applied voltage and a stronger Laplacian field at the same moment on the rising edge of V_a. Therefore, the ionization and excitation become much more intense. The species are also more active, which directly facilitates the ionization and excitation in turn. As a result, the electron density is higher, the current increases more rapidly, and the amplitude is higher.

b. Effect on the inception of volume streamer and the voltage at the breakdown. The volume streamers ignite at 0.9, 1.4, and 1.9 ns,

respectively, with different voltage rising rates, as shown in Fig. 20. The faster voltage rising rate results in earlier ignition of the volume streamer. This is because the electric field can reach the initial field of the volume streamer earlier when the voltage rises faster. It is interesting that the ignition voltage is 4.90, 4.65, and 4.50 kV, respectively, it decreases slightly as the voltage rising rate decreases. In addition, the time when the volume streamer breaks down the gap is 3.8, 4.2, and 4.6 ns, respectively (Fig. 19), and the corresponding voltages are 5.8, 5.5, and 5.3 kV. It can be
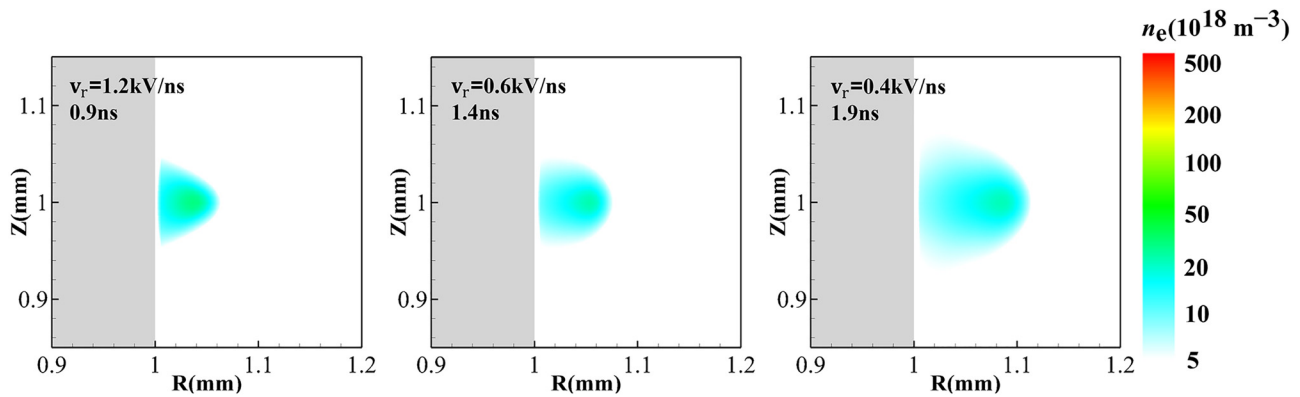
FIG. 20. Electron density distribution at the beginning of discharge with a voltage rising rate of 0.4, 0.6, and 1.2 kV/ns.
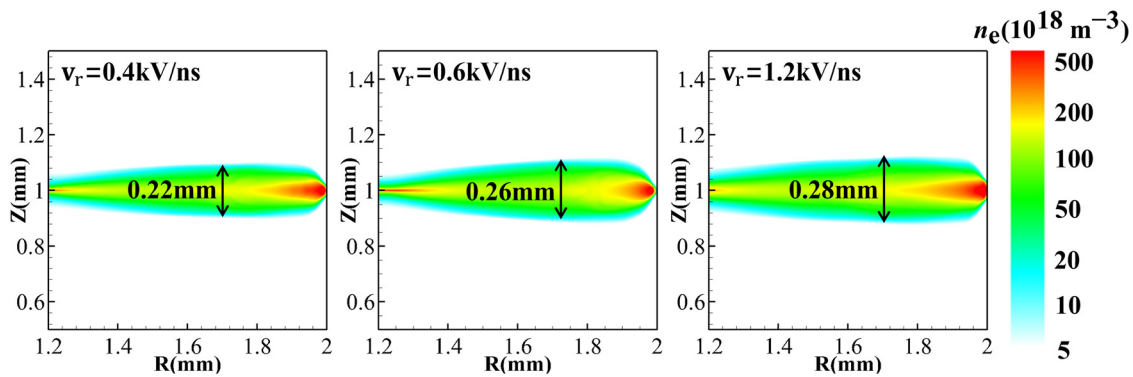

FIG. 21. Electron density distribution at the breakdown with a voltage rising rate of 0.4, 0.6, and 1.2 kV/ns.

concluded that voltage at breakdown increases with the increase in voltage rising rate.

The diameter of the volume streamer is also affected by the rate of voltage rise as shown in Fig. 21; the diameter increases with the increase in the voltage rising rate, which is consistent with Ref. 55. The difference in voltage rise rate is small (they are in the same order of magnitude), so the difference in the diameter is small.

c. Effect on surface streamer velocity. Figure 22 shows that the surface streamer develops faster with an increasing rising rate. As we discussed above, this is because the applied voltage is larger and the reduced electric field is stronger, and the collisions, ionization, and excitation are more intense. A similar dependence of the volume streamer is investigated in a point-to-plane electrode configuration,[54] that the velocity of the volume streamer is faster when the voltage rises faster.
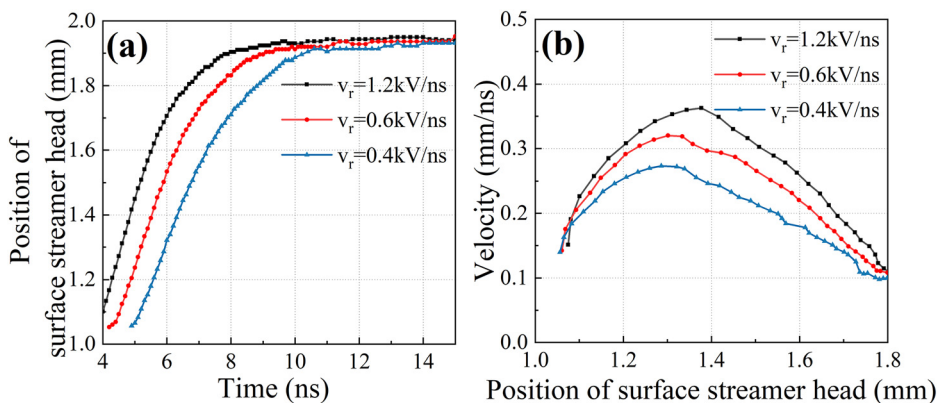

FIG. 22. (a) Position of surface streamer head vs time (b) streamer velocities vs their position with a voltage rising rate of 0.4, 0.6, and 1.2 kV/ns.

In addition, the inflection points occur closer to the collision point ($Z = 1$ mm) when the rise time increases. However, it can be seen that the maximum distance the surface streamer could reach is almost the same in all three cases [Fig. 22(a)].

IV. CONCLUSION

A 2D fluid model is established, and the formation and propagation of pseudo-filamentary dielectric barrier discharge in atmospheric air are investigated. The discharge cell is a coaxial cylinder with an air gap of 1 mm. The pulsed voltage with 6 kV amplitude, 10 ns rise time, and 40 ns full width at half maximum are applied to the high-voltage electrode. The conclusions can be summarized as follows:

(a) Discharge development can be divided into three stages: the volume streamer stage, the surface streamer stage, and the reverse discharge stage. Discharge gradually extinguishes in the surface streamer stage. The reverse discharge is ignited at the falling edge of the applied voltage. And the current peak of the reverse discharge is smaller than that of the first one.

(b) The volume streamer head becomes wider, the velocity is faster, and the electron density increases when the volume streamer interacts with the dielectric. Then, it develops into the surface streamer and propagates in both directions along the dielectric. Surface streamers have a smaller radius, a higher electric field, and a higher electron density, and their velocity increases first and then decreases.

(c) The dielectric permittivity, dielectric thickness, and voltage rising rate have effects on the current density, the inception, and the surface streamer velocity. First, a larger dielectric permittivity, a thinner dielectric, or a faster voltage rise rate leads to a higher current density, because the Laplacian field is stronger in these three cases, which facilitates the ionization and excitation. Second, it leads to the earlier inception of volume streamers, because of the capacitance characteristics of DBD and the evolution of the electric field. The dielectric capacitance C_d becomes larger with a larger dielectric permittivity or a thinner dielectric which enhances the electric field indirectly. And the electric field can reach the initial field of the volume streamer earlier when the voltage rises faster. Third, it also leads to a faster propagation of the surface streamer.

ACKNOWLEDGMENTS

AUTHOR DECLARATIONS
Conflict of Interest

The authors have no conflicts to disclose.

Author Contributions

Yanru Li: Formal analysis (equal); Investigation (lead); Methodology (lead); Writing – original draft (lead); Writing – review & editing (equal). **Yulin Guo:** Methodology (equal); Writing – review & editing (equal). **Yifei ZHU:** Methodology (equal); Software (lead). **Anbang Sun:** Writing – review & editing (supporting).

DATA AVAILABILITY

The data that support the findings of this study are available from the corresponding author upon reasonable request.

REFERENCES

[1] T. Shao, W. Yang, C. Zhang, Z. Niu, P. Yan, and E. Schamiloglu, Appl. Phys. Lett. **105**(7), 071607 (2014).

[2] G. J. Pietsch and V. I. Gibalov, Pure Appl. Chem. **70**(6), 1169–1174 (1998).

[3] V. Narayanaswamy, L. L. Raja, and N. T. Clemens, AIAA J. **48**(2), 297–305 (2010).

[4] Q. Y. Nie, Z. Cao, C. S. Ren, D. Z. Wang, and M. G. Kong, New J. Phys. **11**, 115015 (2009).

[5] X. Lu, Z. Xiong, F. Zhao, Y. Xian, Q. Xiong, W. Gong, C. Zou, Z. Jiang, and Y. Pan, Appl. Phys. Lett. **95**(18), 181501 (2009).

[6] U. Kogelschatz, Plasma Chem. Plasma Process. **23**(1), 1–46 (2003).

[7] M. Kettlitz, H. Höft, T. Hoder, K. D. Weltmann, and R. Brandenburg, Plasma Sources Sci. Technol. **22**(2), 025003 (2013).

[8] N. Merbahi, N. Sewraj, F. Marchal, Y. Salamero, and P. Millet, J. Phys. D **37**(12), 1664–1678 (2004).

[9] M. Laroussi, X. Lu, V. Kolobov, and R. Arslanbekov, J. Appl. Phys. **96**(5), 3028–3030 (2004).

[10] T. Shao, C. Zhang, Y. Yu, Z. Niu, H. Jiang, J. Xu, W. Li, P. Yan, and Y. Zhou, Vacuum **86**(7), 876–880 (2012).

[11] M. Kettlitz, H. Höft, T. Hoder, S. Reuter, K. D. Weltmann, and R. Brandenburg, J. Phys. D **45**(24), 245201 (2012).

[12] R. Brandenburg, Plasma Sources Sci. Technol. **26**(5), 053001 (2017).

[13] R. Brandenburg, H. E. Wagner, A. M. Morozov, and K. V. Kozlov, J. Phys. D **38**(11), 1649–1657 (2005).

[14] S. Jin, Z. Li, Y. Xian, L. Nie, and X. Lu, High Voltage **7**(1), 98–105 (2021).

[15] S. H. Liu and M. Neiger, J. Phys. D **34**(11), 1632–1638 (2001).

[16] Y. V. Yurgelenas and H. E. Wagner, J. Phys. D **39**(18), 4031–4043 (2006).

[17] Y. V. Yurgelenas and M. A. Leeva, IEEE Trans. Plasma Sci. **37**(6), 809–815 (2009).

[18] M. Soo Bak and M. A. Cappelli, J. Appl. Phys. **113**(11), 113301 (2013).

[19] Y. T. Zhang, D. Z. Wang, and Y. H. Wang, Acta Phys. Sin. **54**(10), 4808–4815 (2005).

[20] D. Braun, V. Gibalov, and G. Pietsch, Plasma Sources Sci. Technol. **1**(3), 166–174 (1992).

[21] H. He, D. Xia, B. Luo, W. Chen, K. Bian, and N. Xiang, High Voltage **6**(6), 1079–1091 (2021).

[22] C. Zhang, T. Shao, Y. Yu, Z. Niu, P. Yan, and Y. Zhou, J. Electrost. **68**(5), 445–452 (2010).

[23] A. Laiadi, A. Chentouf, and Y. Laghmich, Mater. Today **24**, 160–165 (2020).

[24] L. Stollenwerk, S. Amiranashvili, J. P. Boeuf, and H. G. Purwins, Phys. Rev. Lett. **96**(25), 255001 (2006).

[25] W. Fan, Z. Sheng, F. Liu, X. Zhong, and L. Dong, Phys. Plasmas **25**(2), 023502 (2018).

[26] Y. Zhu, S. Shcherbanev, B. Baron, and S. Starikovskaia, Plasma Sources Sci. Technol. **26**(12), 125004 (2017).

[27] L. Papageorghiou, E. Panousis, J. F. Loiseau, N. Spyrou, and B. Held, J. Phys. D **42**(10), 105201 (2009).

[28] S. Celestin, Z. Bonaventura, O. Guaitella, A. Rousseau, and A. Bourdon, Eur. Phys. J. Appl. Phys. **47**(2), 22810 (2009).

[29] N. Y. Babaeva and M. J. Kushner, Plasma Sources Sci. Technol. **20**(3), 035017 (2011).

[30] C. Zhang, T. Shao, R. X. Wang, Z. S. Zhou, Y. X. Zhou, and P. Yan, Phys. Plasmas **21**(10), 103505 (2014).

[31] Z. Wang, B. Zhu, and W. Zeng, in *International Technology and Innovation Conference 2006 (ITIC)* (China Academic Journal, 2006), pp. 1165–1169.

[32] G. Fridman, G. Friedman, A. Gutsol, A. B. Shekhter, V. N. Vasilets, and A. Fridman, Plasma Processes Polym. **5**(6), 503–533 (2008).

[33]K. Li, G. Liu, T. Y. Gao, F. Lu, L. H. Tang, S. J. Liu, and P. Ning, Appl. Catal. A **527**, 171–181 (2016).

[34]A. V. Phelps and L. C. Pitchford, Phys. Rev. A **31**(5), 2932–2949 (1985).

[35]N. A. Popov, J. Phys. D **44**(28), 285201 (2011).

[36]S. A. Lawton and A. V. Phelps, J. Chem. Phys. **69**(3), 1055–1068 (1978).

[37]S. Pancheshnyi, M. Nudnova, and A. Starikovskii, Phys. Rev. E **71**(1), 016407 (2005).

[38]I. A. Kossyi, A. Y. Kostinsky, A. A. Matveyev, and V. P. Silakov, Plasma Sources Sci. Technol. **1**(3), 207–220 (1992).

[39]M. Capitelli, C. M. Ferreira, B. F. Gordiets, and A. I. Osipov, *Plasma Kinetics in Atmospheric Gases* (Springer, 2001).

[40]Y. Zhu, X. Chen, Y. Wu, J. Hao, X. Ma, P. Lu, and P. Tardiveau, Plasma Sources Sci. Technol. **30**(7), 075025 (2021).

[41]J. G. Li, Mon. Weather Rev. **136**(12), 4709–4729 (2008).

[42]J. G. Verwer, B. P. Sommeijer, and W. Hundsdorfer, J. Comput. Phys. **201**(1), 61–79 (2004).

[43]A. Bourdon, V. P. Pasko, N. Y. Liu, S. Célestin, P. Ségur, and E. Marode, Plasma Sources Sci. Technol. **16**(3), 656–678 (2007).

[44]O. Schenk and K. Gartner, in *Computational Science-ICCS 2002, Part II, Proceedings*, edited by P. Sloot, C. J. K. Tan, J. J. Dongarra, and A. G. Hoekstra (Springer, 2002), Vol. 2330, pp. 355–363.

[45]P. Sonneveld, SIAM J. Sci. Stat. Comput. **10**(1), 36–52 (1989).

[46]P. L. G. Ventzek, T. J. Sommerer, R. J. Hoekstra, and M. J. Kushner, Appl. Phys. Lett. **63**(5), 605–607 (1993).

[47]A. Villa, L. Barbieri, M. Gondola, and R. Malgesini, J. Comput. Phys. **242**, 86–102 (2013).

[48]Y.-T. Zhang and Y.-H. Wang, Phys. Plasmas **25**(2), 023509 (2018).

[49]A. Zouaghi, A. Mekhaldi, R. Gouri, and N. Zouzou, IEEE Trans. Dielectr. Electr. Insul. **24**(4), 2314–2324 (2017).

[50]S. Schroter, A. Wijaikhum, A. R. Gibson, A. West, H. L. Davies, N. Minesi, J. Dedrick, E. Wagenaars, N. de Oliveira, L. Nahon, M. J. Kushner, J. P. Booth, K. Niemi, T. Gans, and D. O'Connell, Phys. Chem. Chem. Phys. **20**(37), 24263–24286 (2018).

[51]M. Stankov, M. M. Becker, R. Bansemer, K. D. Weltmann, and D. Loffhagen, Plasma Sources Sci. Technol. **29**(12), 125009 (2020).

[52]X. Li, A. Sun, G. Zhang, and J. Teunissen, Plasma Sources Sci. Technol. **29**(6), 065004 (2020).

[53]Y. Wu, Y. Zhu, W. Cui, M. Jia, and Y. Li, Plasma Processes Polym. **12**(7), 642–654 (2015).

[54]A. Komuro, R. Ono, and T. Oda, Plasma Sources Sci. Technol. **22**(4), 045002 (2013).

[55]A. Komuro, T. Ryu, A. Yoshino, T. Namihira, D. Wang, and R. Ono, J. Phys. D **54**(36), 364004 (2021).

30 April 2024 09:25:26